

# Tetraphenylethene-based highly emissive metallacage as a component of theranostic supramolecular nanoparticles

Guocan Yu<sup>a</sup>, Timothy R. Cook<sup>b</sup>, Yang Li<sup>c</sup>, Xuzhou Yan<sup>d</sup>, Dan Wu<sup>c</sup>, Li Shao<sup>a</sup>, Jie Shen<sup>c</sup>, Guping Tang<sup>c</sup>, Feihe Huang<sup>a,1</sup>, Xiaoyuan Chen<sup>e,1</sup>, and Peter J. Stang<sup>d,1</sup>

<sup>a</sup>State Key Laboratory of Chemical Engineering, Center for Chemistry of High-Performance and Novel Materials, Department of Chemistry, Zhejiang University, Hangzhou 310027, People's Republic of China; <sup>b</sup>Department of Chemistry, University at Buffalo, State University of New York, 359 Natural Sciences Complex, Buffalo, NY 14260; <sup>c</sup>Department of Chemistry, Institute of Chemical Biology and Pharmaceutical Chemistry, Zhejiang University, Hangzhou 310027, People's Republic of China; <sup>d</sup>Department of Chemistry, University of Utah, Salt Lake City, UT 84112; and <sup>e</sup>Laboratory of Molecular Imaging and Nanomedicine, National Institute of Biomedical Imaging and Bioengineering, National Institutes of Health, Bethesda, MD 20892

Contributed by Peter J. Stang, October 13, 2016 (sent for review August 12, 2016; reviewed by Jacqueline K. Barton and Alanna Schepartz)

**A theranostic agent combines diagnostic reporter with therapeutic activity in a single entity, an approach that seeks to increase the efficacy of cancer treatment. Herein, we describe the synthesis of a highly emissive tetraphenylethene-based metallacage using multicomponent coordination-driven self-assembly that exhibits a coordination-triggered aggregation-induced emission (AIE) enhancement. The formation of metallacage-loaded nanoparticles (MNPs) occurs when the assembly is treated with two variants of a 1,2-distearoyl-phosphatidylethanolamine (DSPE)/polyethylene glycol (PEG) conjugate, mPEG-DSPE, and biotin-PEG-DSPE. This combination endows the resultant MNPs with excellent stability and targeting ability, specifically enabling selective delivery of the metallacages to cancer cells that overexpress biotin receptors via receptor-mediated endocytosis. Although the mechanism of activity is based on existing Pt(II) anticancer drugs such as oxaliplatin, carboplatin, and cisplatin, *in vitro* and *in vivo* studies indicate that the MNPs are more active and show low systemic activity while also possessing emissive properties that allow for fluorescence-based imaging. This pioneering example of a metallacage that combines biologically active components with AIE imaging establishes supramolecular coordination complexes imbedded within nanoparticles as a promising potential theranostic platform for cancer treatment.**

supramolecular coordination complex | self-assembly | discrete metallacage | theranostic | drug delivery

Over the past decades, platinum-based coordination complexes have been a mainstay of clinical drugs for the treatment of many solid tumors, including testicular, colorectal, genitourinary, and nonsmall cell lung cancers (1, 2). Cisplatin, oxaliplatin, and carboplatin have been approved as first-line chemotherapeutics for the treatment of carcinoma in combination with other anticancer drugs. However, their chemotherapeutic applications are greatly limited by severe side effects that include acute nephrotoxicity, neurotoxicity, ototoxicity, and emetogenesis (3, 4). The search for low-dose platinum-based drugs/prodrugs with high selectivity to tumor tissues motivates the development of targeting drug delivery systems that may reduce side effects and show an improved therapeutic index. Further modifications are sought to address drawbacks of poor solubility, rapid clearance, and a lack of selectivity (5, 6). Although fluorescence-based techniques provide a means to track the processes of translocation, drug release and excretion of anticancer agents, the aforementioned species are intrinsically nonfluorescent under treatment conditions (7–10).

In sharp contrast to the aggregation-caused quenching (ACQ) effect, Tang and colleagues developed a novel class of organic luminogens that are nonemissive in solution but become intensely emissive on aggregation, with pioneering studies based on tetraphenylethene (TPE) and hexaphenylsilole (HPS). This

so-called aggregation-induced emission (AIE) effect is attributed to the restriction of intramolecular rotation (RIR) of the aromatic rings of AIEgens (11). Since the discovery of this phenomenon, it has been used as the basis of biological probes, chemical sensors to fluorescence imaging that all benefit from inherently high sensitivity and contrast, especially for applications requiring concentrations that would cause conventional fluorophores to be quenched. The promise of AIE materials for use in biological settings is tempered by the difficulties associated with the poor cellular uptake of aggregated species and potential blockage of blood vessels. These deleterious effects limit the degree to which fluorophores accumulate at a tumor site, resulting in poor imaging properties. To apply AIE to new theranostic agents, the promising photophysical properties of the luminogens must be preserved in a system that also introduces biological activity and furthermore addresses the need for biocompatibility.

Herein, we report the multicomponent coordination-driven self-assembly of a tetragonal prism (Fig. 1) that occurs when two donor building blocks (1 and 3) are mixed with *cis*-(PEt<sub>3</sub>)<sub>2</sub>Pt(OTf)<sub>2</sub> (2). When combined in a 4:2:8 ratio, precursors 1, 3, and 2 act as the edges, faces, and vertices of the metallacage (4), respectively, under the principles of edge-directed and face-directed directional bonding (12–16). The core of 3 is a TPE moiety whose intramolecular aromatic ring rotation becomes restricted on coordination. The loss

## Significance

Because of severe side effects, poor specificity, and lack of any ability to track the process of translocation, clinic applications of platinum anticancer drugs are limited. New motifs that combine a targeting ability, diagnostic capabilities, and therapeutic functions are urgently needed. Herein, we use a highly emissive metallacage as a component of theranostic supramolecular nanoparticles. *In vitro* and *in vivo* investigations demonstrate the metallacage-loaded nanoparticles (MNPs) are more active and show low systemic activity while also possessing emissive properties that allow for fluorescence imaging. This metallacage provides an excellent nanoplatform on which to develop theranostic anticancer agents, providing a blueprint for the next generation of nanomedicines and the development of noble metal-based-targeted drug delivery systems.

Author contributions: G.Y., F.H., and P.J.S. designed research; G.Y., T.R.C., Y.L., X.Y., D.W., L.S., and J.S. performed research; G.Y., T.R.C., X.Y., L.S., and G.T. analyzed data; and G.Y., T.R.C., X.Y., F.H., X.C., and P.J.S. wrote the paper.

Reviewers: J.K.B., California Institute of Technology; and A.S., Yale University.

The authors declare no conflict of interest.

<sup>1</sup>To whom correspondence may be addressed. Email: stang@chem.utah.edu, fhuang@jzu.edu.cn, or shawn.chen@nih.gov.

This article contains supporting information online at [www.pnas.org/lookup/suppl/doi:10.1073/pnas.1616836113/-DCSupplemental](http://www.pnas.org/lookup/suppl/doi:10.1073/pnas.1616836113/-DCSupplemental).

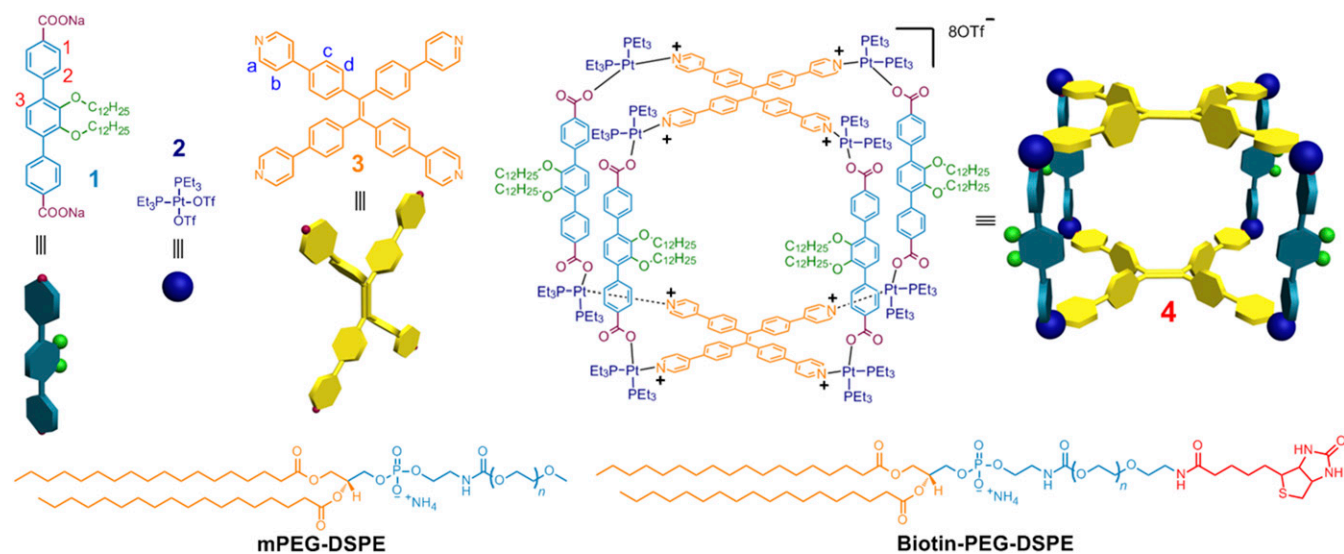


**Fig. 1.** Chemical structures and cartoon representations of the formation of a tetragonal prism **4** from **1–3** and the mPEG-DSPE and biotin-PEG-DSPE agents used for nanoparticle formation.

of this rotation triggers an AIE effect, imparting emissive behavior to the metallacage. Two variants of a 1,2-distearoyl-phosphatidylethanolamine/polyethylene glycol conjugates (mPEG-DSPE and biotin-PEG-DSPE) were used to form nanoparticles within which the metallacage-loaded nanoparticles (MNPs) exhibit excellent stability and targeting ability owing to the PEG and biotin moieties, with the metallacage safely protected within the hydrophobic interior. As discussed below, the MNPs selectively deliver their metallacage payload to cancer cells that overexpress biotin receptor (HeLa and HepG2 cells) over normal cells (CHO and HEK-293 cells) via receptor-mediated endocytosis. In vivo fluorescence imaging indicates that the MNPs show superior fluorescence signal in tumors compared with normal organs, validating their diagnostic capabilities. The presence of Pt(II) ions serving as the metal nodes of **4** provide a mechanism for anticancer activity, resulting in therapeutic functions. Compared with existing Pt(II)-based drugs (oxaliplatin, carboplatin, and cisplatin), the MNPs showed enhanced antitumor activities and low systemic toxicities in a HeLa xenograft mouse model. This increased efficacy is attributed to the enhanced permeability and retention (EPR) effect, followed by receptor-mediated endocytosis.

## Results and Discussion

**Characterizations of MNPs.**  $^{31}\text{P}\{^1\text{H}\}$  NMR,  $^1\text{H}$  NMR, ESI-MS, and 2D diffusion-ordered spectroscopies (DOSYs) were used to establish the successful construction of **4**. Compared with those of the free ligand **3** (*SI Appendix, Fig. S9C*), the signals related to the protons of the pyridyl groups shifted downfield ( $\Delta\delta = -0.22$  and  $-0.34$  ppm for  $\text{H}_a$  and  $\text{H}_b$ , respectively), confirming the coordination of the N atoms to platinum centers (*SI Appendix, Fig. S9B*) (15). Downfield shifts were also observed for the resonances corresponding to the protons on dicarboxylate ligand **1** due to the loss of electron density that occurs on coordination (*SI Appendix, Fig. S9B*) (14). On formation of the tetragonal prism, the resonances in the  $^{31}\text{P}\{^1\text{H}\}$  NMR spectrum shifted significantly upfield from that of the starting Pt(II) acceptor (*SI Appendix, Fig. S9E*). Additionally, the  $^{31}\text{P}\{^1\text{H}\}$  NMR spectrum of **4** contained two doublets of approximately equal intensity at  $\delta = 6.19$  and  $0.77$  ppm ( $^2J_{\text{P-P}} = 20.0$  Hz) with concomitant  $^{195}\text{Pt}$  satellites that correspond to two distinct phosphorous environments. This peak pattern is diagnostic of a multicomponent self-assembly wherein a heteroligated Pt-N,O-coordination motif breaks the symmetry equivalence of the two phosphorous sites (14). The well-defined signals in both the  $^{31}\text{P}\{^1\text{H}\}$  and  $^1\text{H}$  NMR spectra

evidenced the formation of a discrete structure as the sole isolated assembly product. The stoichiometry of formation of **4** was verified by electrospray ionization mass spectroscopy (ESI-MS). As shown in *SI Appendix, Fig. S9F*, the isotopically resolved peaks corresponding to the intact metallacage with the loss of trifluoromethanesulfonate (OTf) anions are found at  $m/z$  2361.2 [**4** – 4 OTf] $^{4+}$  and 1524.5 [**4** – 6 OTf] $^{6+}$ . The isotopic spacing of these peaks is in agreement with their theoretical distributions (16). Moreover, DOSY was carried out to determine the diffusion properties of **4** relative to its building blocks (*SI Appendix, Fig. S9G*). The measured weight average diffusion coefficients ( $D$ ) of the building blocks **1** and **3** were found to be  $6.32 \times 10^{-10}$  and  $6.12 \times 10^{-10} \text{ m}^2 \cdot \text{s}^{-1}$ , respectively. However, the  $D$  value decreased to  $2.03 \times 10^{-10} \text{ m}^2 \cdot \text{s}^{-1}$  on formation of the tetragonal prism, consistent with the significantly larger size of the assembly versus its precursors.

With the metallacage in hand, its photophysical properties were compared with those of **3**. The free donor ligand acted as a classic AIE luminogen, showing weak emission centered at 390 nm when diluted in acetone solution (*SI Appendix, Fig. S10*). The fluorescence intensity of **3** increased significantly when the volume fraction of water ( $f_w$ ) in acetone/water mixtures was increased from 0 to 98 vol%, accompanied by a red shift of the emission maximum to 525 nm (*SI Appendix, Fig. S10*). Whereas **3** is relatively weakly emissive in solution, at equivalent TPE concentration **4** is intensely emissive at  $\sim 525$  nm, the same energy at which **3** manifested its AIE (*SI Appendix, Figs. S11–S13*). The emission of **4** is attributed to the restricted rotation of the aromatic rings of the TPE groups on coordination to the Pt nodes, thus preserving the AIE phenomenon even at low concentrations, in stark contrast to traditional AIE-based fluorogens (17). Compared with free ligand **3**, the fluorescence intensity of **4** was much higher for equal concentrations of TPE groups (*SI Appendix, Fig. S12*). It should be noted that a classic AIE behavior was still observed for **4**. At  $f_w$  values below 80%, the emission intensity was relatively invariant and emission remained strong. However, once the  $f_w$  value exceeded 80 vol%, the emission of **4** began to increase, reminiscent of the classic AIE effect. Compared with the quantum yield (QY) of free **3** (QY = 9% at  $f_w = 98\%$ ), the QY of **4** exhibited a significant enhancement to 39% at the same  $f_w$ .

**In Vitro Cell Imaging and Targeted Delivery.** Nanoparticles (NPs) that are composed of polymers are emerging as a promising platform to develop personalized nanomedicines for disease- and patient-specific diagnosis and treatment (18–23). The ability

to select given surface coatings and grow NPs of controllable size has an effect on the rate of clearance via circulation and immune response, such as the reticuloendothelial system (RES) located in the reticular connective tissue (24–27). mPEG-DSPE and biotin-PEG-DSPE were used to incorporate **4** into MNPs whose terminal biotin groups would provide selective transport to cancer cells overexpressing biotin receptors (28). The Tyndall effect was observed for MNP suspensions, indicating the formation of self-assembled aggregates (*SI Appendix*, Fig. S15B). Transmission electron microscopy (TEM) and dynamic light scattering (DLS) techniques were used to establish the size and morphology of the MNPs. As shown in *SI Appendix*, Fig. S15A, solid spherical structures with an average diameter of  $\sim 35$  nm were observed in the TEM image. From a magnified image of these nanostructures, no sharp color contrast between the periphery and central parts was observed, consistent with the formation of micellar NPs. In DLS experiments, a unimodal peak distribution with an effective average hydrodynamic diameter of  $38 \pm 4.7$  nm was observed (*SI Appendix*, Fig. S15B), in good agreement with the results obtained from TEM and SEM images (*SI Appendix*, Fig. S15C). The existence of Pt in the MNPs was confirmed by energy dispersive spectrometry (EDS) to support that **4** was incorporated into the micellar assemblies (*SI Appendix*, Fig. S16). The tetragonal prisms structure of **4** was maintained in the core of the MNPs (*SI Appendix*, Fig. S17). Furthermore, the *in vitro* stability of the MNPs was evaluated in PBS buffer supplemented with 10% (vol/vol) FBS at 37 °C. No obvious size variation was observed over 20 h, confirming the excellent stability of these MNPs (*SI Appendix*, Fig. S18).

Confocal laser scanning microscopic (CLSM) and flow cytometry (FCM) investigations were carried out to confirm that the biotin-functionalized MNPs were selectively guided to cancer cells that overexpressed receptors (HeLa and HepG2 cells) over normal cells (CHO and HEK-293 cells). As shown in Fig. 2, the HeLa (Fig. 2A) and HepG2 (Fig. 2B) cells exhibited strong intracellular fluorescence after incubation with the MNPs for 2 h, and the fluorescence intensity became much stronger when the incubation time was extended to 4 h. The CHO (Fig. 2D) and HEK-293 (Fig. 2C) cells showed only a weak fluorescence signal under the same experimental conditions. The extent to which the MNPs internalized into the cells was quantified by FCM experiments summarized in Fig. 2E–H. HeLa (Fig. 2E) and HepG2 (Fig. 2F) cells show a higher rate of uptake and higher intracellular accumulations than CHO and HEK-293 cells (Fig. 2G and H). These results are consistent with the hypothesis that an overexpression of biotin receptors on the HeLa and HepG2 cells results in better uptake, ultimately leading to a greater fluorescence signal. CLSM analyses showed that the green fluorescence signal arising from **4** was observed in the same regions as the blue fluorescence signal

from the DAPI stain (Fig. 2A and B), indicating that the TPE-based ligand was delivered to and accumulated in the nucleus. As such, the Pt content within the nucleus versus the cytoplasm was quantified indicating that  $\sim 99\%$  of metal was accumulated in the nucleus (*SI Appendix*, Table S1). After internalization, the metal-lacages were deconstructed in the endo/lysosomes at relatively low pH. We hypothesize that the resultant fragments containing Pt(II) and TPE groups accumulated in the cell nucleus due to the coordination between the N<sub>7</sub> atoms of purine bases on DNA and the Pt centers (4). <sup>1</sup>H NMR spectra (*SI Appendix*, Fig. S25) and viscometry experiments (*SI Appendix*, Fig. S26) provided direct evidence for the interaction between Pt(II) and DNA. To further verify this hypothesis, HeLa and HepG2 cells were cultured with the NPs containing **3** (*SI Appendix*, Fig. S20). CLSM images show that the green fluorescence is observed in the cytoplasm (*SI Appendix*, Fig. S21–S24), which indicates that the free **3** is distributed in the lysosomes, thus confirming that the existence of Pt(II) is responsible for the accumulation of the resultant fragments in the nucleus.

To further probe if the increased uptake of **4** in the tumor cell lines was due to the biotin targeting groups or some secondary effect of the MNPs, a competition experiment was designed. HeLa and HepG2 cells were pretreated with an excess of biotin for 2 h before incubation with the MNPs, thus occupying the receptors. CLSM (Fig. 2A and B) and FCM (Fig. 2E and F) analysis of the pretreated cells revealed that the fluorescence intensity in the HeLa and HepG2 lines decreased significantly compared with that observed for the biotin-untreated cells. Because cellular uptake is blocked when the receptors are occupied, these results strongly support a mechanism wherein the MNPs enter via receptor-mediated endocytosis and suggest that biotin-PEG-DSPE is a critical component of the NPs.

The cytotoxicities of building blocks **1–3** and the MNPs were evaluated by a 3-(4',5'-dimethylthiazol-2'-yl)-2,5-diphenyl tetrazolium bromide (MTT) assay with concentrations ranging from 10 to 200  $\mu$ M. The relative cell viability was not significantly altered in this concentration range (*SI Appendix*, Fig. S27), suggesting low cytotoxicity of **1** and **3**. However, **2** showed high cytotoxicity toward cells both rich and poor in biotin receptors, indicating that a receptor-mediated pathway was not active for the monomeric Pt(II) complex. The anticancer activity of **2** toward the cell lines is attributed to their ability to form intra- and interstrand cross-links on DNA via coordination of the N<sub>7</sub> atoms of purine bases to the platinum centers. In sharp contrast to results obtained for CHO and HEK-293 cells, the MNPs exhibited significantly enhanced dose-dependent anti-proliferative activity against HeLa and HepG2 cells (*SI Appendix*, Fig. S27). The enhanced cytotoxicity of the MNPs toward HeLa and HepG2 cells provides further support for a targeted, biotin-mediated uptake of the MNPs.

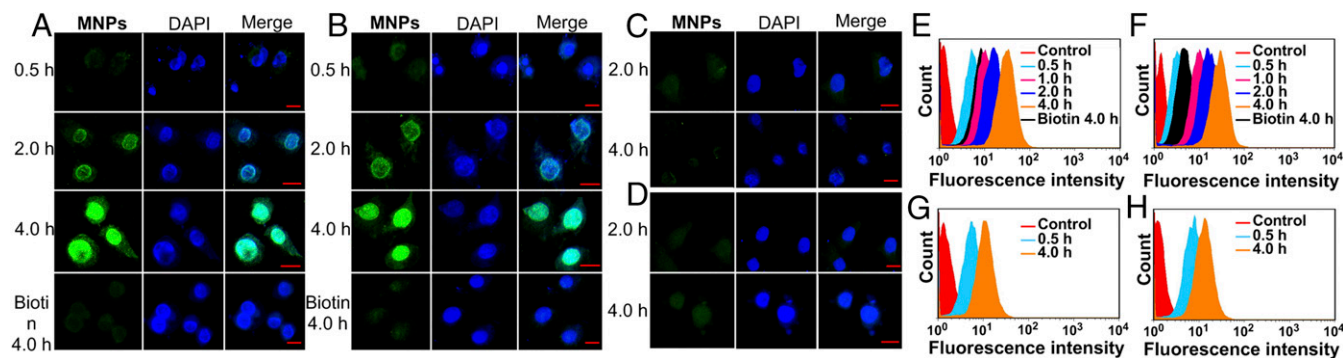


**Fig. 2.** Confocal microscopy images of (A) HeLa, (B) HepG2, (C) HEK-293, and (D) CHO cells incubated with the MNPs. Nucleus stained with DAPI (blue). Red bar indicates 20  $\mu$ m in the images. Flow cytometry analysis results of fluorescence signals collected in (E) HeLa, (F) HepG2, (G) HEK-293, and (H) CHO cells after treatment with the MNPs in the absence and presence of biotin for different time periods. Cells without any treatment were regarded as control groups.

As was seen in the uptake experiments, the activity decreased significantly on pretreatment with biotin before incubating with the MNPs, in this case manifesting in higher viabilities at all concentrations. However, the difference in cytotoxicity in the treated and untreated CHO and HEK-293 cells was negligible, offering evidence that HeLa and HepG2 draw on a receptor-mediated uptake that is absent in the HEK-293 and CHO lines. Moreover, the cytotoxicity of the metallacage-loaded NPs fabricated from mPEG-DSPE without biotin groups toward HeLa and HepG2 cells was much lower than that treated with MNPs under the same conditions (SI Appendix, Fig. S29C), further providing convincing evidence for the receptor-mediated endocytosis of MNPs.

Inductively coupled plasma mass spectrometry (ICP-MS) was used to determine the amount of platinum internalized by the cells incubated with MNPs. On the basis of ICP-MS measurements, the accumulation of Pt in HeLa and HepG2 cells was determined to be 7.12 and 6.86 ng/10<sup>6</sup> cell, respectively, after a 4-h incubation with MNPs, a roughly twofold increase over the CHO and HEK-293 cells under the same conditions (SI Appendix, Fig. S28). Analogous experiments using cells pretreated with biotin or the metallacage-loaded NPs without biotin groups were also carried out (SI Appendix, Fig. S29B), resulting in a significant decrease in the Pt content for HeLa and HepG2 cells in these experiments, in full accord with similar results obtained from CLSM, FCM, and the MTT assays. To have a more complete understanding of the cellular response induced by MNPs, we evaluated their mode of cell death using an Annexin V-FITC/PI flow cytometry assay (SI Appendix, Table S2). To eliminate the influence of fluorescence arising from **4** that is similar to that of FITC, we chose **2** as a model compound to further determine the percentage of apoptotic cells. Compound **2** induced large populations of HeLa (16.7% for early apoptosis; 10.0% for later apoptosis; 2.40% for necrosis), and HepG2 cells (14.8% for early apoptosis, 9.19% for later apoptosis, and 2.33% for necrosis) to undergo early- and late-stage apoptosis,

possibly as a result of *cis*-(PEt<sub>3</sub>)<sub>2</sub>Pt(OTf)<sub>2</sub>-induced damage to the apoptotic program (4).

**Theranostic Functions of MNPs In Vivo.** HeLa tumor-bearing female nude mice were used to assess the in vivo theranostic potential of the MNPs. Mice administered with oxaliplatin, carboplatin, or cisplatin were used as controls. The ~37-nm size of the MNPs studied here falls within the optimal range for tumor targeting and penetration via the so-called enhanced permeability and retention (EPR) effect established for poorly permeable cervical cancer models, in which nanoscopic species are particularly prone to uptake due to the leaky vasculature of the system. To establish the circulation time of these MNPs, we evaluated the pharmacokinetics following i.v. injection in normal mice and analyzed the Pt content in plasma by ICP-MS at various time points. The circulation half-life of the MNPs was much higher than those of oxaliplatin, carboplatin, and cisplatin, confirming that MNPs possessed a longer blood circulation time than the control drugs (Fig. 3A), leading to enhanced efficacies over traditional Pt(II) agents.

To quantitatively determine the distribution of Pt in tissue, oxaliplatin, carboplatin, cisplatin, or MNPs were injected i.v. into HeLa tumor-bearing nude mice. At 24 (Fig. 3B) and 48 h (Fig. 3C) postinjection, the amount of Pt in tumor tissue and normal organs was measured by ICP-MS to probe for selective accumulation of the MNPs. Significant accumulation of Pt from the nanoparticles in the tumor was observed in comparison with clinical formulations of oxaliplatin, carboplatin, or cisplatin as expected from the prolonged circulation time and enhanced internalization of MNPs as established in the previously discussed experiments. Moreover, administration of MNPs resulted in a lower Pt uptake by the liver, spleen, lung, and kidneys, which suggested that the use of PEGylated MNPs could decrease the systemic toxicity of drug to normal tissues/organs.

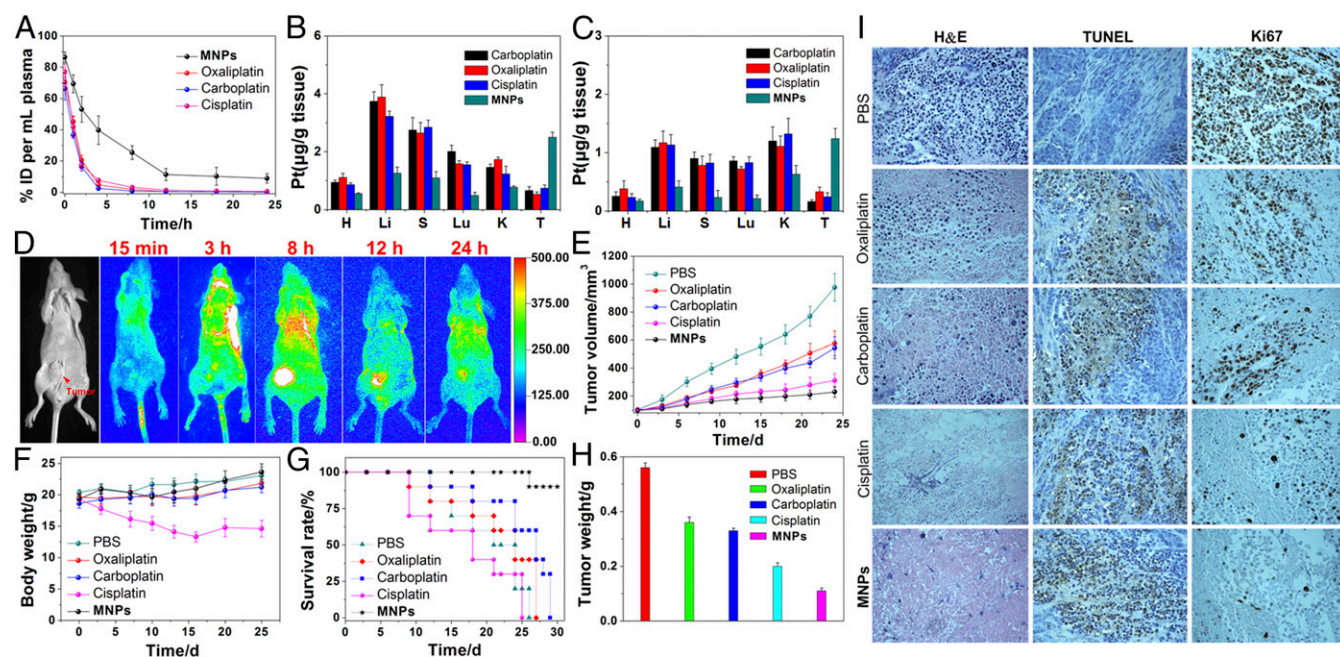


**Fig. 3.** (A) In vivo blood elimination kinetics of oxaliplatin, carboplatin, cisplatin, and the MNPs at a dose of 2 mg Pt per kilogram body weight ( $n = 3$  for each group). Tissue distributions of the Pt in the main organs after i.v. injection of oxaliplatin, carboplatin, cisplatin, or MNPs for (B) 12 h and (C) 24 h. (H, heart; Li, liver; S, spleen; Lu, lung; and K, kidney). (D) Representative in vivo fluorescence imaging of nude mice bearing HeLa cancer xenograft following i.v. injection of MNPs. (E) In vivo tumor growth inhibition curves for PBS, oxaliplatin, carboplatin, cisplatin, or MNPs on the HeLa tumor model. (F) Average body weights of tumor-bearing mice injected with the different formulations. (G) Kaplan–Meier plots showing the percentage of animals remaining in the study. (H) The average weight of the tumors was assessed after the last determination. (I) H&E, TUNEL, and Ki67 analyses of tumor tissues after treatment with various formulations. Ki67-positive or TUNEL-positive tumor cells were stained brown.

The intense fluorescence of the MNPs enabled imaging techniques to monitor the pharmacokinetics in HeLa tumor-bearing mice. A sustained systemic distribution of MNPs was observed after i.v. injection, indicating the ability of MNPs to effectively avoid particle opsonization and removal by the mononucleosis phagocytosis system. The fluorescence signal of localized MNPs at tumor tissues gradually increased with time (Fig. 3D). In vivo fluorescence imaging at 8 h postinjection showed that the MNPs had higher fluorescence signal at tumor site compared with normal organs. This signal persisted, even at postinjection times as long as 24 h, with a significant biodistribution of the MNPs throughout the specimen. The passive targeting of tumors by MNPs was attributed to its prolonged circulation times, which significantly enhanced the permeability and retention of the MNPs in the tumor. In contrast, the fluorescence signal in the body annihilated much faster and no targeting phenomenon was observed for the mice after administration of the NPs fabricated from **3** (SI Appendix, Fig. S30), confirming the longer blood circulation and targeting delivery of the PEGylated MNPs to tumor tissue through the EPR effect (Fig. 4).

The ability for the MNPs to selectively deliver active Pt(II) agents and inhibit tumor growth was next explored with in vivo experiments wherein the xenograft tumor growth of HeLa cancer following i.v administration of MNPs was monitored with a dose of 2 mg platinum per kilogram of mouse body weight. As shown in Fig. 3E, the control group treated with PBS did not show any noticeable inhibition of tumor growth. Administration of free oxaliplatin or carboplatin resulted in a slight inhibition of tumor growth and no differences were observed between the oxaliplatin- and carboplatin-treated groups. Although treatment with cisplatin led to more significant inhibition of tumor growth compared with oxaliplatin and carboplatin, the MNPs were most effective in treating HeLa tumor-bearing mice. Our results demonstrated that in vivo targeted delivery of the platinum anticancer drug using the MNPs was more effective for the treatment of HeLa tumors compared with conventional oxaliplatin, carboplatin, or cisplatin treatment (SI Appendix, Fig. S31).

Using loss of body weight as an indication of systemic toxicity, the body weight of MNPs-treated mice was not significantly different from that of mice in the PBS control group (Fig. 3F), and even a slight enhancement of body weight was observed during the period of drug administration. However, the mice treated with free cisplatin exhibited significant weight loss during the experimental period. These data support an in vivo biocompatibility of the MNPs and indicate a reduction of the systemic toxicity commonly

associated with Pt(II) agents. Histological analyses showed that nephrotoxicity and pulmonary and hepatic damage were observable for the oxaliplatin or carboplatin treatment, especially for the cisplatin treatment (SI Appendix, Fig. S32). The systemic toxicity of the MNPs was effectively reduced as H&E staining revealed no apparent tissue damage or morphological changes in the normal organs following treatment. The Kaplan–Meier survival plots of treated mice are shown in Fig. 3G. At day 25, 27, and 29, all mice treated with cisplatin, oxaliplatin, and carboplatin were dead, likely due to the previously mentioned damage in these organs induced by Pt(II) agents. In contrast, MNPs treatment significantly prolonged the survival of the mice, further confirming that MNPs have low systemic toxicity arising from greatly reduced delivery of Pt(II) to normal tissue compared with tumor sites. Moreover, tumor masses were excised after the last measurements, and the average weight of the tumors was assessed. As expected, the weight of the tumor mass was the lowest after treatment with MNPs (Fig. 3H), confirming our newly developed theranostic nanomaterial exhibited the improved efficacy for cancer therapy with lower systemic toxicity, compared with the free anticancer drugs.

Cell proliferation and apoptosis in the tumor tissue were analyzed by H&E staining assay after treatment with various formulations. As shown in Fig. 3I, all treated groups showed varying levels of necrosis compared with the PBS-treated group, suggesting that all of the applied drug formats possess antitumor properties. Among these therapeutic groups, the tumor tissues from treatment with the MNPs showed the fewest tumor cells and the highest level of tumor necrosis, indicating massive remission of proliferative activity. The extent of apoptosis in tumor cell lines was compared across treatments with Pt agents and further determined using the transferase-mediated dUTP nick end-labeling (TUNEL) staining. The tumor tissue of the mice treated with MNPs revealed much higher apoptotic levels than the groups treated with PBS, oxaliplatin, carboplatin, and cisplatin (Fig. 3J). Moreover, Ki67-positive immunohistochemical staining was used, where cell proliferation was denoted as brown spots in the captured images (Fig. 3I). The Ki67-positive cells were prevalent in mice treated with PBS. The oxaliplatin-, carboplatin-, or cisplatin-treated groups showed fewer Ki67-positive tumor cells using the same methods, and the MNPs treatment group revealed the greatest reduction of Ki67-positive tumor cells. Taken together, these experimental data clearly demonstrate an enhanced efficiency of MNPs for inhibiting proliferation and inducing the apoptosis of tumor cells.

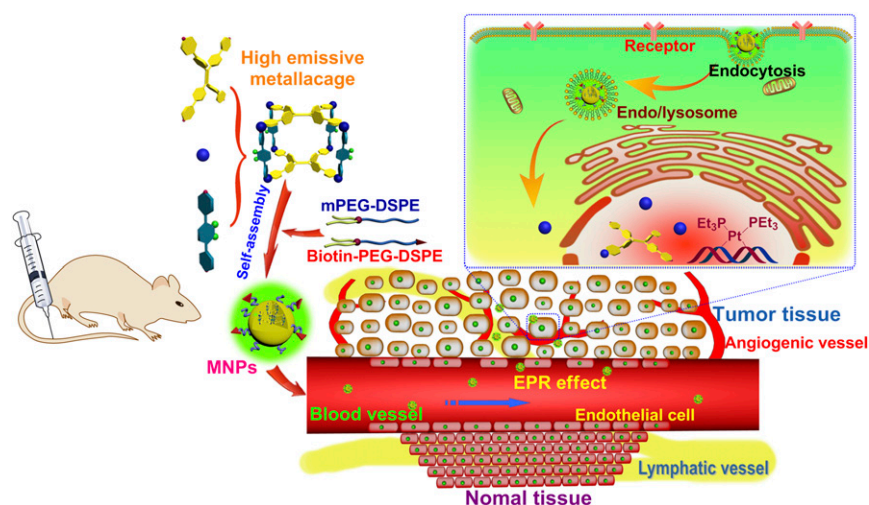


Fig. 4. Scheme of MNPs transportation within blood vessels and accumulation in tumor tissue, followed by receptor-mediated endocytosis.

## Conclusion

In summary, we prepared a theranostic system with the capability to perform dual functions (i.e., imaging and therapy) by unifying self-assembly, coordination chemistry, and supramolecular chemistry. By incorporating AIE luminogens into a building block for coordination-driven self-assembly of a tetragonal prismatic metallacage, fluorescence was triggered even at concentrations wherein the free ligand was nonemissive, attributed to a restriction of intramolecular rotations on coordination. The metallacage was then prepared for biological environments by encapsulation within spherical micelles formed from a mixture of mPEG-DSPE and biotin-PEG-DSPE, wherein the presence of polyethylene glycol and biotin groups provided a means to stabilize the prisms sitting safely within the hydrophobic pocket. These theranostic nanoparticles demonstratively combine diagnostic and therapeutic functions and actively target the biotin receptor-positive cancer cells selectively over biotin receptor-negative cells. In vivo investigations demonstrated that the MNPs possess higher antitumor efficacy with lower toxicity compared with free platinum anticancer drugs (oxaliplatin, carboplatin, and cisplatin). This metallacage provides an excellent nanoplatform on which to develop theranostic anticancer agents, providing a blueprint for the next generation of nanomedicines and the development of noble metal-based targeted drug delivery systems.

## Materials and Methods

All reagents were commercially available and used as supplied without further purification. Deuterated solvents were purchased from Cambridge Isotope Laboratory. The  $^1\text{H}$  NMR and  $^{13}\text{C}$  NMR spectra were recorded on a Bruker Avance DMX-500 spectrometer or on a Bruker Avance III-400 spectrometer with internal standard tetramethylsilane (TMS). DOSY spectra were collected on a Bruker Avance DMX-500 spectrometer with internal standard TMS. The  $^{31}\text{P}\{^1\text{H}\}$  NMR chemical shifts are referenced to an external unlocked sample of 85%  $\text{H}_3\text{PO}_4$ . The fluorescence experiments were conducted on a RF-5301 spectrofluorophotometer (Shimadzu). Mass spectra were recorded on

a Micromass Quattro II triplequadrupole mass spectrometer using electrospray ionization (Bruker-Franzen Analytik). High-resolution mass spectrometry experiments were performed with a Bruker 7-Tesla FT-ICR mass spectrometer equipped with an electrospray source (Billerica). The melting points were collected on a SHPSIC WRS-2 automatic melting point apparatus. SEM investigations were carried out on a Multimode 8 instrument operating at an energy of 15 K or 20 K. TEM investigations were carried out on a HT-7700 instrument.

**Fabrication of the Metallacage.** *Cis*-Pt( $\text{PEt}_3$ ) $_2$ (OTf) $_2$  (9.79 mg, 13.4 mM), **1** (4.91 mg, 6.72 mM), and **3** (2.15 mg, 3.36 mM) were placed in a 2-dram vial, followed by addition of  $\text{D}_2\text{O}$  (0.2 mL) and acetone- $d_6$  (0.8 mL). After 3 h of heating at 75 °C, all solvent was removed by  $\text{N}_2$  flow and then dried under vacuum. Acetone- $d_6$  (0.7 mL) was then added into each mixture. A clear solution was obtained after an additional 5 h of heating at 75 °C. The metallacage was precipitated with diethyl ether, isolated, and dried under reduced pressure. This precipitation–redissolve procedure was repeated three times, and then the metallacage was dissolved in  $\text{CD}_2\text{Cl}_2$  for characterization.

**Preparation of MNPs.** The nanoparticles containing the metallacages were prepared via the matrix-encapsulation method. Briefly, 1 mL of acetone solution containing mPEG-DSPE (25.0 mg), biotin-PEG-DSPE (5.00 mg), and **4** (4.00 mg) was injected into 20 mL of MilliQ water, followed by sonication of the mixture for 90 s at 18 W output. The mixture was then stirred at 600 rpm at room temperature in the dark for 72 h for the evaporation of acetone. After passing through a 0.2- $\mu\text{m}$  syringe filter, the MNPs suspension was obtained and stored at room temperature for further use.

**Other Methods.** All experiments involving live animals were approved by the Zhejiang University Animal Care and Use Committee. The details of the synthesis and characterization are given in *SI Appendix*.

**ACKNOWLEDGMENTS.** Financial support was provided by National Science Foundation Grant 1212799 (to P.J.S.); National Basic Research Program Grant 2013CB834502; National Natural Science Foundation of China Grants 21125417, 21434005, and 21620102006; the Fundamental Research Funds for the Central Universities; Key Science Technology Innovation Team of Zhejiang Province Grant 2013TD02; and Open Project of State Key Laboratory of Supramolecular Structure and Materials Grant sklssm201509 (to F.H.).

- Farrell NP (2015) Multi-platinum anti-cancer agents. Substitution-inert compounds for tumor selectivity and new targets. *Chem Soc Rev* 44(24):8773–8785.
- Klein AV, Hambley TW (2009) Platinum drug distribution in cancer cells and tumors. *Chem Rev* 109(10):4911–4920.
- Wu B, Drøge P, Davey CA (2008) Site selectivity of platinum anticancer therapeutics. *Nat Chem Biol* 4(2):110–112.
- Wang D, Lippard SJ (2005) Cellular processing of platinum anticancer drugs. *Nat Rev Drug Discov* 4(4):307–320.
- Jung Y, Lippard SJ (2007) Direct cellular responses to platinum-induced DNA damage. *Chem Rev* 107(5):1387–1407.
- Kelland L (2007) The resurgence of platinum-based cancer chemotherapy. *Nat Rev Cancer* 7(8):573–584.
- Wilson JJ, Lippard SJ (2014) Synthetic methods for the preparation of platinum anticancer complexes. *Chem Rev* 114(8):4470–4495.
- Liu D, Poon C, Lu K, He C, Lin W (2014) Self-assembled nanoscale coordination polymers with trigger release properties for effective anticancer therapy. *Nat Commun* 5:4182–4192.
- Wang X, Wang X, Guo Z (2015) Functionalization of platinum complexes for biomedical applications. *Acc Chem Res* 48(9):2622–2631.
- Grishagin IV, et al. (2014) *In vivo* anticancer activity of rhomboidal Pt(II) metallacycles. *Proc Natl Acad Sci USA* 111(52):18448–18453.
- Mei J, Leung NLC, Kwok RTK, Lam JWY, Tang BZ (2015) Aggregation-induced emission: Together we shine, united we soar! *Chem Rev* 115(21):11718–11940.
- Cook TR, Stang PJ (2015) Recent developments in the preparation and chemistry of metallacycles and metallacages via coordination. *Chem Rev* 115(15):7001–7045.
- Chakrabarty R, Mukherjee PS, Stang PJ (2011) Supramolecular coordination: Self-assembly of finite two- and three-dimensional ensembles. *Chem Rev* 111(11):6810–6918.
- Yan X, Cook TR, Wang P, Huang F, Stang PJ (2015) Highly emissive platinum(II) metallacages. *Nat Chem* 7(4):342–348.
- Wang M, Zheng YR, Ghosh K, Stang PJ (2010) Metallosupramolecular tetragonal prisms via multicomponent coordination-driven template-free self-assembly. *J Am Chem Soc* 132(18):6282–6283.
- Ye Y, et al. (2015) Self-assembly of chiral metallacycles and metallacages from a rationally adaptable BINOL-derived donor. *J Am Chem Soc* 137(37):11896–11899.
- Ding D, Li K, Liu B, Tang BZ (2013) Bioprobes based on AIE fluorogens. *Acc Chem Res* 46(11):2441–2453.
- Torchilin VP (2014) Multifunctional, stimuli-sensitive nanoparticulate systems for drug delivery. *Nat Rev Drug Discov* 13(11):813–827.
- Song J, Huang P, Duan H, Chen X (2015) Plasmonic vesicles of amphiphilic nanocrystals: Optically active multifunctional platform for cancer diagnosis and therapy. *Acc Chem Res* 48(9):2506–2515.
- Peer D, et al. (2007) Nanocarriers as an emerging platform for cancer therapy. *Nat Nanotechnol* 2(12):751–760.
- Allen TM, Cullis PR (2004) Drug delivery systems: Entering the mainstream. *Science* 303(5665):1818–1822.
- Ferrari M (2005) Cancer nanotechnology: Opportunities and challenges. *Nat Rev Cancer* 5(3):161–171.
- Obermeier B, Wurm F, Mangold C, Frey H (2011) Multifunctional Poly(ethylene glycol)s. *Angew Chem Int Ed Engl* 50(35):7988–7997.
- Knop K, Hoogenboom R, Fischer D, Schubert US (2010) Poly(ethylene glycol) in drug delivery: Pros and cons as well as potential alternatives. *Angew Chem Int Ed Engl* 49(36):6288–6308.
- Nicolas J, Mura S, Brambilla D, Mackiewicz N, Couvreur P (2013) Design, functionalization strategies and biomedical applications of targeted biodegradable/bio-compatible polymer-based nanocarriers for drug delivery. *Chem Soc Rev* 42(3):1147–1235.
- Wang D, Zhao T, Zhu X, Yan D, Wang W (2015) Bioapplications of hyperbranched polymers. *Chem Soc Rev* 44(12):4023–4071.
- Davis ME, Chen ZG, Shin DM (2008) Nanoparticle therapeutics: An emerging treatment modality for cancer. *Nat Rev Drug Discov* 7(9):771–782.
- Kumar R, et al. (2015) Small conjugate-based theranostic agents: An encouraging approach for cancer therapy. *Chem Soc Rev* 44(19):6670–6683.